Arch. Metall. Mater. **71** (2026), 1, 117-131

DOI: https://doi.org/10.24425/amm.2026.157775

XUE-MEI WANG[1], QING-DONG ZHONG[1,2*], LAN MA[2], YU-CHENG YU[2], SHU-JIAN ZHANG[1], BIN XIE[1]

INVESTIGATION OF THE CORROSION BEHAVIOR OF COPPER-NICKEL ALLOY/CARBON STEEL COUPLE UNDER ARTIFICIAL DEFECTS IN EPOXY COATINGS EXPOSED TO SULFIDE-CONTAMINATED SEAWATER

The corrosion behavior of copper-nickel alloy/carbon steel couple, subjected to a sulfide-containing simulated seawater environment beneath an artificially defective epoxy coating, was systematically investigated using a combination of wire beam electrode (WBE), electrochemical impedance spectroscopy, and microscopic characterization techniques. The results indicate that the anodic reaction at the artificial defect during the early stages of immersion is the most intense. A broad spectrum of cathodic currents is observed at the coating/metal interface. As immersion time progresses, the artificial defects are progressively protected by the corrosion product iron sulfide, resulting in a gradual attenuation of the anodic reaction. A significant disparity in the degree of cathodic delamination exists between coupled copper-nickel alloy and carbon steel beneath the epoxy coating. It can be attributed to their different electrochemical activities and the specific location of the artificial defect on the WBE. Throughout the immersion process, the copper-nickel alloy is less eroded. This phenomenon can be attributed to the protective effect of copper oxide and basic copper chloride films and the microgalvanic effect. In the region of carbon steel, multiple anodes are positioned at the immersed end. In addition, the reasons why individual carbon steel electrodes exhibit polarity reversal vary at different immersion stage.

Keywords: Copper-nickel alloy; Carbon steel; Sulfide; Epoxy coating; Polarity reversal

1. Introduction

B18 copper-nickel alloy is extensively utilized in seawater cooling systems due to its exceptional thermal conductivity, robust anti-pollution properties, and superior corrosion resistanc [1-3]. The corrosion resistance of B18 can be attributed to the presence of a double-layer corrosion product film on its surface. The inner layer predominantly consists of a cuprous oxide film incorporating Ni^{2+} and Fe^{2+}, while the outer layer is primarily composed of a thick, porous film of Cu (II) hydroxide/oxide/hydroxychloride [4,5]. In real-world operational conditions, offshore engineering equipment inevitably comes into contact with dissimilar metals. Due to the mechanical performance and cost considerations associated with offshore platform construction, A36 structural steel is commonly employed as a support material [6]. The complexity of the operational environment renders such contact phenomena prone to induce galvanic corrosion of metals, thus compromising the safety of marine engineering equipment [7].

The aggressive marine environment exerts a profound impact on the corrosion behavior of metallic materials, primarily governed by microbial contamination, environmental stress, and various external factors [8,9]. Sulfide contamination in seawater may arise from several sources, including bacterial reduction of naturally occurring sulfates, decaying vegetation, and the discharge of industrial waste [10]. In polluted harbors and estuaries, fresh aerated seawater is typically introduced by tidal movements twice daily. The concentration of inorganic sulfur in offshore port waters surpasses that of natural seawater by several orders of magnitude [11,12]. Consequently, the corrosion of copper-nickel alloys and carbon steel in sulfide-contaminated seawater is influenced. Habib et al. [13] examined the impact of temperature and sulfide concentration on the stress corrosion cracking (SCC) susceptibility of 90/10 and 70/30 copper-nickel alloys in natural seawater. Both alloys exhibit susceptibility to SCC in seawater contaminated with sulfides at moderate temperatures. With a gradual increase in sulfide concentration from 200 ppm S^{2-} to 3120 ppm S^{2-}, the susceptibility of the 70/30 copper-nickel alloy to SCC at 25°C becomes more pronounced. Li et al. [3] explained that the corrosion product film on the 70/30 copper-nickel alloy in sulfide-containing seawater consists of a double-layer

[1] SHANGHAI UNIVERSITY, SCHOOL OF MATERIALS SCIENCE AND ENGINEERING, STATE KEY LABORATORY OF ADVANCED SPECIAL STEEL, SHANGHAI 200444, CHINA
[2] PANZHIHUA UNIVERSITY, PANZHIHUA, SICHUAN 61700, CHINA

* Corresponding author:qdzhong@shu.edu.cn

structure: a loose, porous sulfur-containing outer layer and a dense inner layer. It has been proposed that sulfides inhibit the formation of Cu_2O, a protective oxide layer on the alloy surface. Goldman et al. [14] demonstrated that low concentrations of sulfide (10^{-6} M) facilitated the anodic dissolution of carbon steel in a carbonate solution. The presence of sulfide destabilizes the formation of Fe (III) oxide by competing for surface adsorption sites on iron and chemically reducing Fe (III) oxide. Reactions between Fe (III) and sulfides lead to the formation of elemental sulfur, sulfates, and polysulfides. The presence of polysulfides can promote the formation of pyrite (FeS_2).

As an in-situ electrochemical technique, wire beam electrode (WBE) enables real-time monitoring of current fluctuations on metal surfaces during corrosion processes. It can be employed to investigate the electrochemical distribution in complex systems and to analyze the phenomena and severity of corrosion, thereby offering a robust tool for studying galvanic corrosion. Numerous researchers have noted that WBE can effectively form couples for experimental simulations of galvanic corrosion in multi-metal complex coupling systems, which, though rarely reported, are widely prevalent. Ju et al. [15] employed WBE technology to examine the local electrochemical properties of three coupled metals in seawater desalination systems. HAl77-2 aluminum brass wire serves as the anode, undergoing corrosion within the three-metal coupling system. TA2 titanium wire functions as the cathode and is protected, while 316L stainless steel wire serves as the secondary cathode. This observation demonstrates that WBE technology can monitor the dynamic progression of galvanic corrosion. Kou et al. [16] provided an in-depth discussion on the advancements of WBE technology in studying the evolution of corrosion processes and polarity reversal in marine environments. Zhang et al. [17] employed WBE to investigate the galvanic effects of deposited and bare electrodes in CO_2-containing formation water. The current map generated by WBE revealed that severe localized corrosion occurred on the electrode covered by the deposited layer.

Organic coatings function as a physical barrier between the metal surface and corrosive media, thereby extending the service life of metal components and widely employed to mitigate metal corrosion [18-22]. However, limited studies have been conducted on the galvanic corrosion behavior of dissimilar metals under organic coatings in marine environments. Xie et al. [18,20] employed WBE in conjunction with electrochemical impedance spectroscopy (EIS) to investigate and found that the degree of cathodic stratification of WBE in flowing seawater was higher than in static seawater, primarily due to the cathodic reduction reaction in flowing seawater. When artificial defects are present on the surface of carbon steel, the degree of cathodic delamination of the coating in the carbon steel region is higher. Sykes et al. [23,24] demonstrated that, during the onset of galvanic corrosion of zinc/steel under an organic coating, the anode and cathode are located at different positions. Throughout the wet-dry cycle, interfacial current persists. The impedance of a coating exhibits variable behavior depending on the metal substrate. To date, limited research has been conducted on the failure behavior and mechanisms of dissimilar metal-organic coatings in sulfide-contaminated marine environments. Therefore, it is imperative to investigate the corrosion behavior of dissimilar metals under organic coatings in sulfide-containing environments.

In this paper, WBE, EIS and microscopic characterization techniques were used to study the corrosion behavior of coupled copper-nickel alloy and carbon steel under an organic coating with artificial defects in sulfide-containing artificial simulated seawater. The distribution of current density and the evolution of EIS characteristics of dissimilar metals as a function of immersion time were analyzed. The reasons for the difference in the degree of cathodic delamination of the two metals under the organic coating were discussed. The surface morphological characteristics observed through WBE were analyzed, and the polarity reversal of the single carbon steel/copper-nickel alloy electrode was investigated. Furthermore, X-ray photoelectron spectroscopy analysis was conducted to examine the corrosion products. The failure mechanism of the coating/metal system in the sulfide environment was further revealed.

2. Experimental procedures

2.1. Materials and test solutions

The WBE consists of 100 wires of B18 copper-nickel alloy with a diameter of 1 mm and A36 carbon steel. The composition of the two metals is shown in TABLE 1. The two wires each constitute 50% of the total assembly. The assembly is sealed with black epoxy resin in a 10×10 configuration. The electrodes are spaced 1 mm apart and are electrically insulated from one another. The WBE was prepared as shown in Fig. 1(a). To remove the original oxide layer from the surface of the WBE prior to coating, the samples were pretreated with 400# and 800# SiC sandpaper, followed by cleaning with deionized water and ethanol. The epoxy coating applied in this experiment was sourced from Baijiatu Co., Ltd., and is specifically designed to provide strong adhesion to the substrate. The primary raw materials for the coating consist of epoxy resin and 740 hardener in a 4:1 volume ratio. Coating defects were introduced by masking the surface of the No. 55 and 56 electrodes before coating, with a hole diameter of 1 mm. To ensure uniform coating thickness across the WBE, the epoxy resin was applied to the electrode surface in a single application. After application, the WBE was air-dried at room temperature (23 ± 3°C) for 24 h, followed by drying in a 70°C oven for 48 h. The coating thickness after full curing was measured using the NT-1 thickness gauge, with the dry film thickness found to be 100 ± 10 μm. The area measured in this study corresponds to the area of a single WBE, with a value of 7.85×10^{-3} cm^2.

The solution employed in this study consisted of 3.5 wt.% sodium chloride (NaCl) with sulfide. The addition of sodium sulfide nonahydrate ($Na_2S \cdot 9H_2O$) created a simulated sulfide-bearing seawater environment. The survey revealed that in environments subjected to contamination, the sulfide concentration typically spans from 0 to 20 mg/L [3,11]. The initial

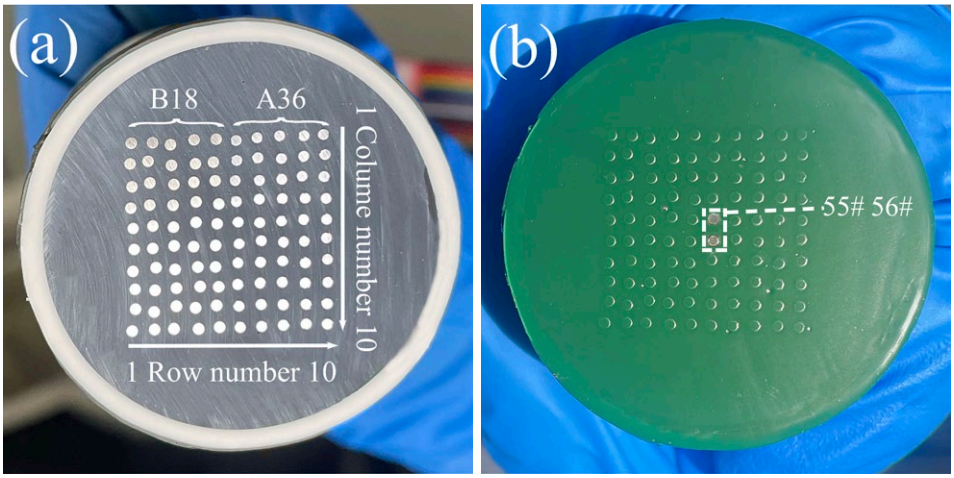

Fig. 1. Surface of the wire beam electrode prepared after coupling B18 copper-nickel alloy and A36 carbon steel: (a) the uncoated; (b) the epoxy-coated with artificial defect

sulfide concentration employed in this study was approximately 10 mg/L. All experiments were conducted at room temperature and standard atmospheric pressure.

TABLE 1

Chemical compositions of B18 copper-nickel alloy and A36 carbon steel

Materials	Element (wt.%)								
	C	Mn	Si	P	S	Ni	Zn	Cu	Fe
B18	/	0.82	0.15	/	/	17.58	0.30	Bal.	1.17
A36	0.25	0.82	0.21	0.01	0.005	/	/	/	Bal.

2.2. Electrochemical measurements

The WBE scanner (CST 520, Wuhan Corrtest Instrument Co., Ltd.) comprises a 10×10 array of scanning circuits (Auto switch), a high-impedance conversion module, an automatic measurement system, a data storage unit, and a data output/display unit. The entire measurement process is controlled by a microcontroller, and 100 low-power relays facilitate the automatic cyclic potential/current scanning of 100 electrodes. The built-in electronic switch enables automatic switching of the potential/current range for the WBE. The test data are automatically calculated and transmitted to the host computer. The use of a disturbance-free current scanning mode allows the WBE scanning technology to accurately reflect the local corrosion state of the metal beneath the coating. The instrument employs a zero-resistance current mode for current measurements. The test principles are illustrated in Fig. 2. The input impedance is 1×10^{12} Ω, and the maximum measurable current range is ±20 mA. The working electrode consists of 100 wires, with the saturated calomel electrode (SCE) serving as the reference

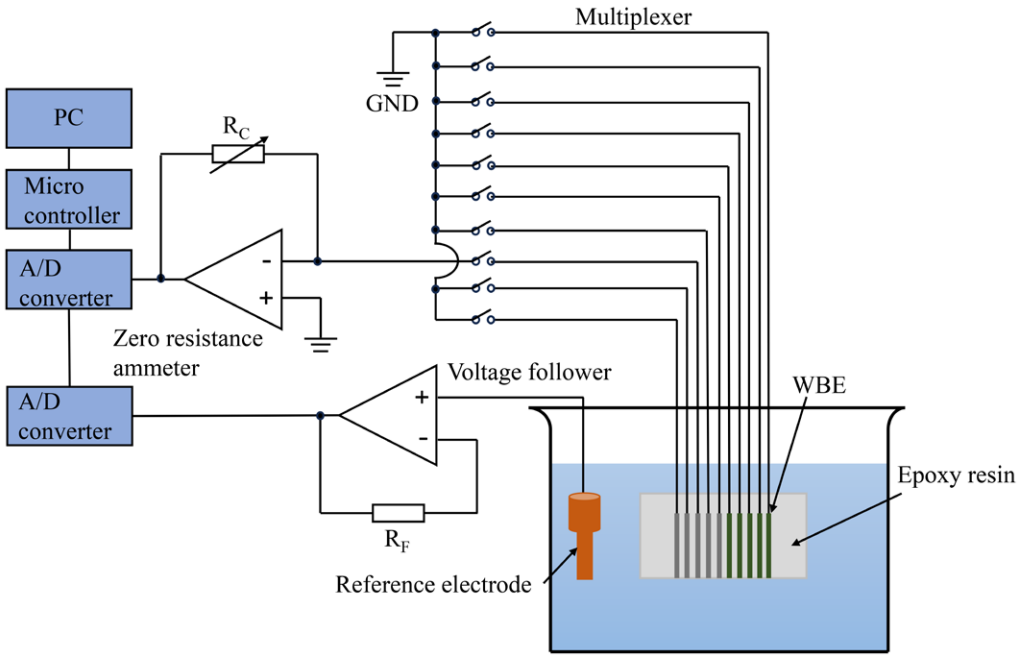

Fig. 2. Working principle schematic diagram of wire beam electrode (WBE)

electrode. All wires are interconnected prior to current measurement. Once the current distribution measurement begins, a single electrode is disconnected from the others, and the current between the electrode and the remaining electrodes is recorded. The testing process is then repeated. A total of 100 seconds is required to complete a current sweep of the WBE. The current density distribution was plotted using Origin 2024 software.

The EIS tests were conducted on two distinct materials under the coating using an electrochemical testing system (CS 350, Wuhan Corrtest Instrument Co., Ltd.). All tests were conducted at open circuit potential (OCP). The electrochemical cell employs a three-electrode system. The WBE serves as the working electrode, with a platinum sheet as the counter electrode and the SCE as the reference electrode. The test frequency range spans from 10 kHz to 10 mHz, with a sinusoidal excitation signal featuring a 20 mV. For EIS measurements in the carbon steel region under organic coatings, 48 carbon steel electrodes were coupled, excluding electrodes No. 55 and 56. After completing the EIS measurements for the two materials, all electrodes in the WBE are re-coupled. The EIS data were analyzed using ZsimpWin 3.6 software. All tests in this study were conducted in triplicate to ensure data reliability.

2.3. Surface morphology and component analysis

To assess the tightness of the epoxy coating, a water absorption test was conducted prior to WBE measurements. Initially, the coating sample was weighed to determine its baseline mass (W_1 = 14.27 g), after which it was immersed in deionized water for 24 hours. The temperature is controlled at 23±2°C. Following immersion, the sample was carefully wiped to remove surface moisture and reweighed (W_2 = 14.39 g). The water absorption rate was then calculated using the equation:

$$\frac{W_2 - W_1}{W_1} \times 100\% = 0.84\% \quad (1)$$

The test is repeated at least three times, leaving off values that exceed 10% of the average. According to the relevant industry standards, such as JC/T 2663-2022 (Test method for water absorption of building water proofing membrane), HG/T 4758-2014 (Water-based acrylic resin coatings), water absorption rate below 2% indicates satisfactory coating tightness [25,26]. Furthermore, the coating exhibits a uniform appearance with no visible particulate defects, further verifying its sealing effectiveness, as illustrated in the Fig. 3.

A digital camera was employed to monitor the macroscopic morphology of the WBE surface as it was immersed in a sulfide-containing NaCl solution over time. The chemistry of the corrosion products was analyzed using an X-ray photoelectron spectroscopy (XPS, Thermo Fisher Scientific K-Alpha, USA).

3. Results and discussion

3.1. Current density distributions of the WBE

The current density distribution of the WBE at various immersion times is presented in Fig. 4. Due to inaccuracies in the measurement time of the current density distribution, data were collected for WBE immersion times of 0.5 h, 24 h, 72 h, 144 h, 216 h, 288 h, 360 h, and 432 h. Upon exposure of the WBE to sulfide-containing NaCl solution for 0.5 h, distinct anode current peaks were observed at electrodes No. 55 and 56, with peak values reaching 796 μA/cm^2 and 320 μA/cm^2, respectively. This phenomenon is primarily attributed to the rapid reaction of Fe^{2+} on the metal surface with HS^-/H^2S, the details of which are discussed in Section 3.3. Excluding the electrode at the artificial defect, the anode current range in the WBE was confined to a few microamperes. This suggests that, apart from electrodes No. 55 and 56, the remaining electrodes in the WBE were not corroded, owing to the protective effect of the epoxy coating. Cathodic currents exhibit a range from a few microamperes to several tens of microamperes. It is evident that the cathodic current density on the surface of B18 is markedly higher, which may be attributed to the galvanic coupling effect between carbon steel and copper-nickel alloy, favoring the promotion of B18 as the cathode. The current density of individual WBE electrodes differs significantly from that of the other electrodes, indicating

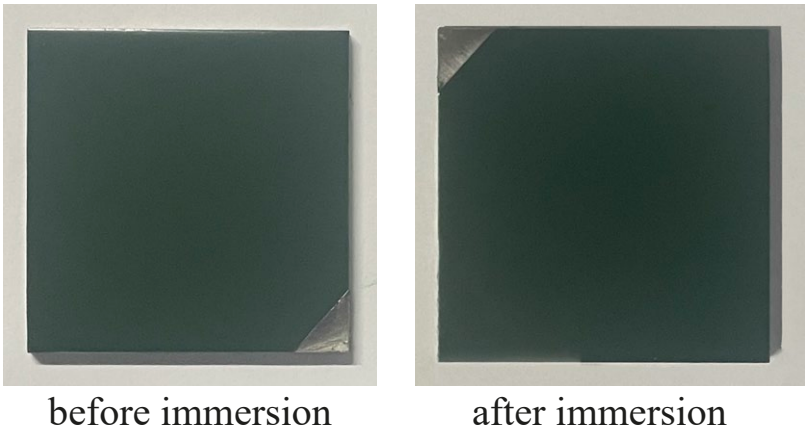

Fig. 3. Optical images captured before and after immersion

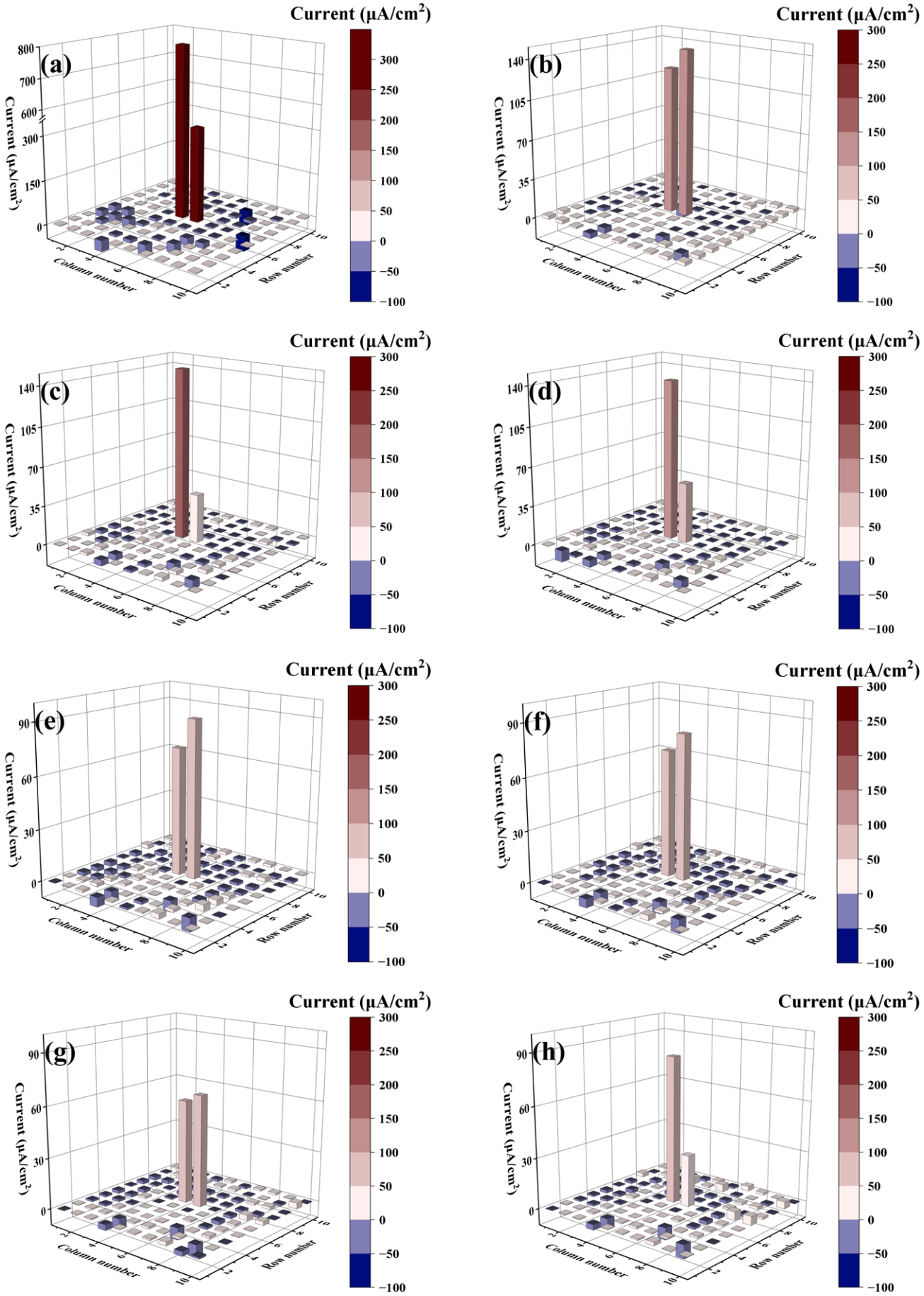

Fig. 4. Current density distributions of wire beam electrode under different immersion time: (a) 0.5 h; (b) 24 h; (c) 72 h; (d) 144 h; (e) 216 h; (f) 288 h; (g) 360 h; (h) 432 h

the electrochemical inhomogeneity between the carbon steel and copper-nickel alloys beneath the coating during galvanic corrosion [18,20].

The peak anode currents at electrodes No. 55 and 56 on the WBE surface decreased after 24 h of immersion, as shown in Fig. 4(b). This decrease is primarily attributed to the formation of a protective iron sulfide (FeS) film on the surface [27,28]. The cathode current density at the coating/metal interface decreased. The anode current on the A36 surface is slightly increased, which may be due to the degradation of the coating. After 72 h and 144 h of immersion, the anode current of electrode No. 55 remained stable at approximately 140 μA/cm^2. The current density at the No. 56 anode decreased to approximately 50 μA/cm^2. This reduction can be attributed to the compactness of the corrosion products.

The anodic current of electrodes No. 55 and 56 progressively decreased with increasing immersing time, while cathodic current peaks emerged and dissipated at various electrode surfaces over different soaking periods. It is noteworthy that the cathodic current density observed on the A36 surface remains consistently low. Following the soaking of the terminal, multiple significant anodic currents were observed in the carbon steel region beneath the coating. Individual electrodes (e.g., No. 59, 60, 90) transition from cathodic to anodic behavior, resulting in a reversal of polarity. The degradation of the organic coating can be effectively reflected by the shift in the position of the primary cathode. The variation in the position of the primary cathode with soaking time is illustrated in Fig. 5. The cathode centers on the surface of the WBE are widely distributed, with the number of cathode centers in the carbon steel region being significantly higher than that in the copper-nickel alloy region [18,20]. This phenomenon is primarily associated with the electrochemical behavior of the metal, as well as the spatial location of the coating defect on the WBE.

3.2. EIS characteristics of the WBE

The resistance of the corrosion products reflects their ability to protect the metal matrix. EIS serves as a nondestructive technique for assessing surface resistance by analyzing the electrochemical system's response to an alternating current perturbation. The EIS curves of WBE immersed in sulfide-containing NaCl solution for varying durations are shown in Fig. 6. The Nyquist plot of B18 at various immersion times, both at high and low frequencies, displays capacitive arcs, as shown in Fig. 6(a). Generally, a larger capacitive arc diameter and higher impedance correspond to better protective effects on the substrate [29]. With increasing immersion time, the diameter of the initial capacitive arc resistance at high frequency exhibited a trend of first decreasing, then increasing. However, the observed differences are minimal, suggesting that the epoxy coating provides effective protection to the substrate. The low-frequency capacitive arc shifts to the high-frequency range with increasing immersion time. Similarly, the phase angle in the Bode plot increases progressively at low frequencies. Notably, the Nyquist plot after 0.5 h of immersion exhibits a low-frequency diffusion tail. It is well known that the Warburg diffusion impedance appears as a 45◦ tail in the Nyquist plot and as a −45° slope of |Z| in the low-frequency region in the Bode plot [30]. The presence of Warburg suggests that the diffusion process is a crucial control step in the electrode reaction. The results indicate that the corrosion mechanism is governed by both the charge transfer and diffusion processes. The EIS curve of B18 was fitted with an appropriate equivalent circuit, as shown in Fig. 7. In the equivalent circuit, R_s represents the solution resistance, Q_{ec} is an epoxy coating constant phase angle element, R_{ec} denotes the epoxy coating impedance, Q_{dl} corresponds to the double layer capacitance, and R_{ct} is the charge transfer resistance; W represents the Warburg

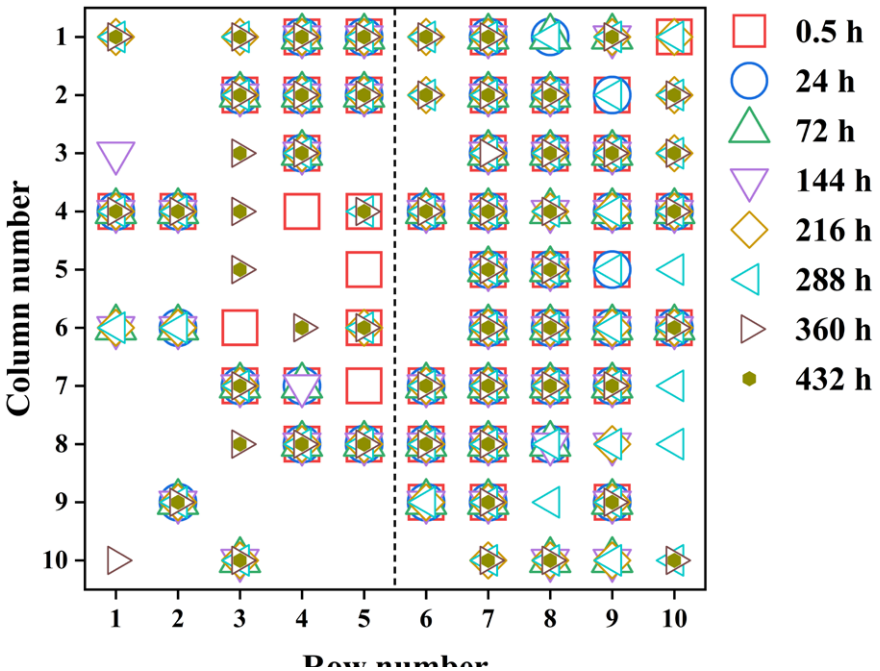

Fig. 5. Schematic diagram of main cathode position changes with immersion time

impedance. Constant phase elements (CPE), calculated according to Eq. (2), were employed to describe non-ideal capacitance and to mitigate the "dispersion effect" caused by surface inhomogeneity of the epoxy coatings [31].

$$Q = \left[Y_0 (j\omega)^n \right]^{-1} \tag{2}$$

where Q denote the magnitude of CPE, Y_0 represents the admittance modulus ($s^n \cdot \Omega^{-1} \cdot cm^{-2}$), j represents the imaginary unit ($j^2 = -1$), ω the angular frequency, n is a constant with a value between 0 and 1. Notably, the fitted n value of the CPE after immersion for 24 h to 432 h in the low-frequency region approaches 0.5, indicative of the inhomogeneity of charge transfer at the coating/metal interface [32-34]. The EIS fitting results for different metals at varying immersion times under the epoxy coating system are presented in TABLE 2. The R_{ec} on the surface of B18 initially decreases and then increases with prolonged immersing time. However, the changes are minimal, suggesting that the protective properties of the coating remain effective. In the later stages of immersion, the R_{ct} increases by more than a dozen orders of magnitude, with no Warburg diffusion phenomenon observed. The results indicate that the cathodic reaction under the epoxy coating is primarily governed by the charge transfer step, with minimal production. Overall, the B18 matrix remains well-protected throughout the immersion process.

The EIS curves for A36 (excluding electrodes No. 55 and 56) immersed in sulfide-containing NaCl solution for varying durations are shown in Fig. 6(c)-(d). The Nyquist curves at all immersion stages exhibit capacitance arcs at high frequencies and sloping lines at low frequencies. The circuit model of the coating at each immersion stage in the sulfide-containing solution incorporates Warburg elements, indicating that the chemical reaction at the coating/metal interface promotes diffusion by facilitating the removal of the binder phase in the coating. The electrochemical reaction area at the coating/metal interface is minimal, complicating the separation of the temporal relaxation of the physical impedance of the coating from that of the electrochemical reaction impedance at the coating/metal interface [20,35]. Consequently, in the Nyquist plot, the second capacitance loop is small and may not be observable. The EIS results for A36 were fitted to an appropriate equivalent circuit, as shown in Fig. 7(b). The presence of three time constants at each immersion stage indicates that the coating degrades as the cathodic reduction reaction on the carbon steel surface persists, leading to distinct and separate time constants that characterize the corrosion reaction at both the coating and coating/metal interface. The Nyquist diagram reveals that the capacitive arc diameter at high frequency progressively decreases with increased immersion time, suggesting that the protective effect of the coating on the substrate weakens. The |Z| film value in Bode diagram is also

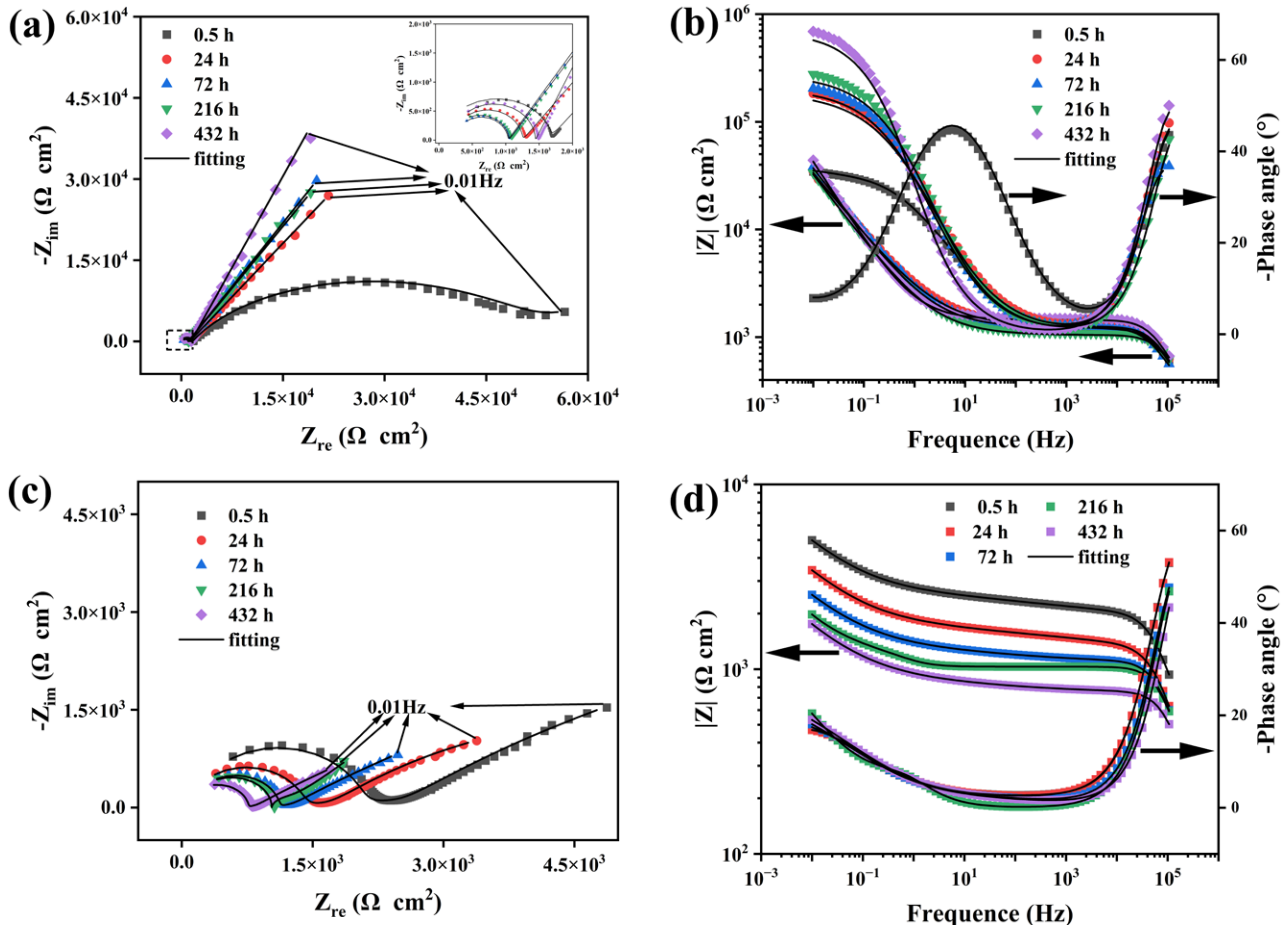

Fig. 6. Electrochemical impedance spectroscopy data under different immersion time in epoxy coating system: (a, b) copper-nickel alloy; (c, d) carbon steel

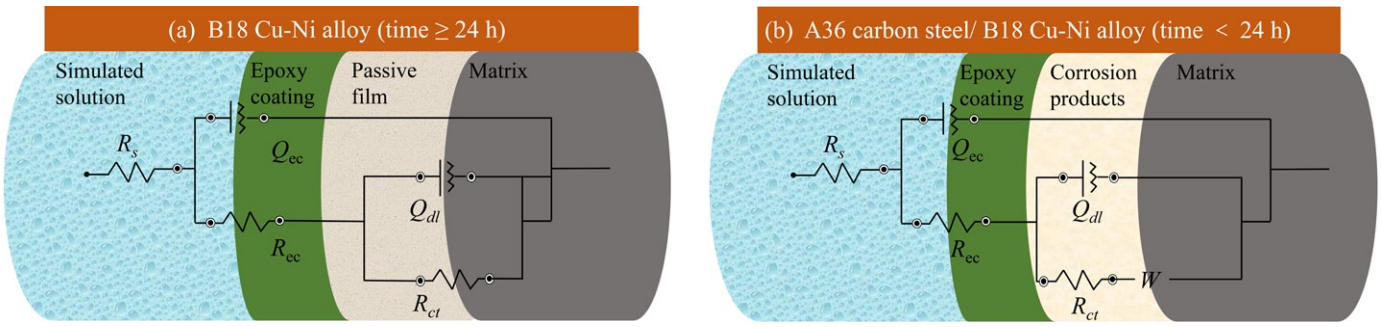

Fig. 7. Equivalent circuits used to fit the obtained electrochemical impedance spectroscopy

getting smaller and smaller. This is consistent with the observation that a significant anode current appears on the surface of A36 during the later stages of immersion in WBE, excluding artificial defects. The fitted EIS results are presented in TABLE 2. As the immersing time increased, the impedance in the carbon steel region beneath the epoxy coating progressively decreased. Under identical immersing conditions, the impedance value of the carbon steel region was substantially lower than that of the copper-nickel alloy region, suggesting a higher degradation rate of the epoxy coating in the carbon steel region. This provides compelling evidence supporting the notion that the galvanic coupling effect between the carbon steel region and the copper-nickel alloy region accelerates the corrosion of the carbon steel surface.

3.3. Corrosion mechanism induced by artificial defects

In the initial stage of immersion, the rapid dissolution of carbon steel leads to the production of a substantial amount of Fe^{2+} on the metal surface. The resulting chemical reaction is as follows [36,37]:

$$Fe \rightarrow Fe^{2+}_{sol} + 2e^{-} \quad (3)$$

In a NaCl solution containing sulfide, the action of sodium sulfide (Na_2S) may lead to the formation of hydrogen sulfide (H_2S). The potential chemical reactions are as follows [12,28]:

$$2Na^{+} + S^{2-} \rightarrow Na_2S \quad (4)$$

$$S^{2-} + H_2O \rightarrow HS^{-} + OH^{-} \quad (5)$$

$$HS^{-} + H_2O \rightarrow H_2S + OH^{-} \quad (6)$$

Under specific conditions, the presence of H_2S can mitigate the corrosion of iron. One proposed mechanism for the dissolution of iron in aqueous solutions containing H_2S involves the formation of FeS. The potential reactions that may occur are as follows [17,28,38]:

$$Fe^{2+} + HS^{-} \rightarrow FeS + H^{+} \quad (7)$$

$$Fe^{2+} + H_2S \rightarrow FeS + 2H^{+} \quad (8)$$

The Fe^{2+} ions on the metal surface undergo a rapid reaction with HS^{-}/H_2S in the surrounding solution, leading to a substantial acceleration of the corrosion rate, which ultimately culminates in the formation of insoluble FeS. The formation of FeS predominantly occurs as a result of its role as a reduction site, thereby enhancing the rate of the anodic reaction [8,14]. The FeS scale formed during corrosion can serve as a barrier, effectively retarding further corrosion and influencing the subsequent mass transfer processes [28,38]. This phenomenon explains the relatively high anodic current density observed at the artificial defects (electrodes No. 55 and No. 56) after an immersion period of 0.5 h. In contrast, the remaining A36 electrodes, which are covered by the coating, predominantly exhibit cathodic currents. This behavior may be attributed to the production of OH^{-} ions

TABLE 2

The fitting results of the electrochemical impedance spectroscopy of B18 copper-nickel alloy and A36 steel in chloride solutions containing sulfide

Time (h)	Materials	$R_s \times 10^2$ ($\Omega \cdot cm^2$)	$Q_{ec} \times 10^{-4}$ ($\Omega^{-1} \cdot cm^{-2} \cdot s^n$)	n_{dl}	$R_{ec} \times 10^3$ ($\Omega \cdot cm^2$)	$Q_{dl} \times 10^{-4}$ ($\Omega^{-1} \cdot cm^{-2} \cdot s^n$)	n_{dl}	$R_{ct} \times 10^2$ ($\Omega \cdot cm^2$)	$W \times 10^{-3}$ ($\Omega^{-1} \cdot cm^{-2} \cdot s^{0.5}$)
0.5	B18	7.10	8.07×10^{-6}	1	3.49	0.14	0.70	1.12×10^5	0.25
	A36	6.10	1.08×10^{-5}	1	4.67	3.16	0.30	5.18	4.13
24	B18	2.06	1.53	0.58	1.04	1.54	0.59	1.10×10^{12}	/
	A36	1.92	2.38×10^{-5}	1	1.30	0.39	0.12	5.04	3.54
72	B18	2.92	1.55	0.62	0.93	1.56	0.53	4.83×10^{12}	/
	A36	1.23	2.40×10^{-5}	1	0.96	9.71	0.28	4.27	2.92
216	B18	1.83	1.88	0.82	0.86	1.80	0.53	7.41×10^{13}	/
	A36	1.07	2.47×10^{-5}	1	0.92	8.68	0.95	2.16	2.12
432	B18	1.96	1.80	0.73	1.25	1.81	0.58	7.64×10^{13}	/
	A36	0.97	4.92×10^{-5}	0.93	0.69	5.33	0.31	1.67	1.19

via oxygen reduction and S^{2-} hydrolysis within the epoxy coating in the sulfide-containing NaCl solution, which leads to the successful passivation of the carbon steel matrix and limits the mass transfer processes of metal ions [3,22]. The corresponding oxygen reduction reaction is illustrated below [39]:

$$O_2 + 2H_2O + 4e^- \rightarrow 4OH^- \quad (9)$$

Additionally, the Fe^{2+} ions generated by anodic dissolution can react with Cl^- ions to form ferric chloride ($FeCl_3$)/ferrous chloride ($FeCl_2$). Given the minimal impact of this reaction on the overall corrosion process, the role of Cl^- ions at the surface of the A36 electrode is not addressed in this study. When the concentration product of Fe^{2+} and OH^- exceeds the solubility limit of ferrous hydroxide ($K_{sp} = [Fe^{2+}] \times [OH^-]^2$), the formation and deposition of $Fe(OH)_2$ crystals occur on the metal surface, indicating that the saturation level (S) of $Fe(OH)_2$ exceeds unity [37,39]:

$$Fe^{2+} + 2OH^- \rightarrow Fe(OH) \quad (10)$$

$$S_{Fe(OH)_2} = \frac{\alpha_{Fe^{2+}} \times \alpha_{OH^-}}{K_{sp,Fe(OH)_2}} \quad (11)$$

Consequently, due to the rapid formation of FeS during the initial immersion period and the subsequent influence of $Fe(OH)_2$, the diffusion of dissolved oxygen, which is integral to the cathodic reaction, faced increasing impediments. This resulted in the attenuation of the oxygen reduction reaction on the electrode surface beneath the epoxy coating after 24 h of immersion. This ultimately led to a decrease in the cathodic current density at the coating/metal interface, which in some instances, reversed into anodic current. Simultaneously, owing to the protective role of the coating, the anode current density remained within the microampere range. XPS analysis of the corrosion products at the artificial defects was performed, with the fitting results displayed in Fig. 9(a). The XPS results indicate that the fitted peaks of Fe $2p_{3/2}$ at 710.3 eV and 713.2 eV binding energy (BE) are both attributable to FeS [8,40]. The Fe $2p_{3/2}$ satellite peak further confirms the presence of Fe^{2+} [41]. As demonstrated in the S 2p spectrum shown in Fig. 9(b), the BE at 162.5 eV suggests that the predominant valence state of sulfur in the film is S^{2-} [8]. The SO_4^{2-} peak (with a BE ranging from 168 to 170 eV) is likely attributed to the deposition of sulfate on the surface. The possible chemical reactions involved are as follows [14]:

$$HS^- \rightarrow S_2^{2-} \rightarrow S_2O_3^{2-} \rightarrow SO_4^{2-} \quad (12)$$

As the immersion time extends (72 h and 144 h), the $[Fe^{2+}] \times [OH^-]^2$ precipitate undergoes a reaction with oxygen in the electrolyte, resulting in the formation of γ-FeOOH. XPS analyses were conducted on the surface corrosion products during this immersion period. The fitting results are presented in Fig. 9(c). The fitting peak of Fe $2p_{3/2}$ at 711.5 eV is assigned to γ-FeOOH [40]. The potential chemical reactions involved are outlined below [39]:

$$4Fe(OH)_2 + 2H_2O + O_2 \rightarrow 4Fe(OH)_3\downarrow \quad (13)$$

$$Fe(OH)_3 \rightarrow \gamma\text{-FeOOH}\downarrow + H_2O \quad (14)$$

The overall reaction network involved in the artificial defects within 0-144 h of immersion is shown in Fig. 8.

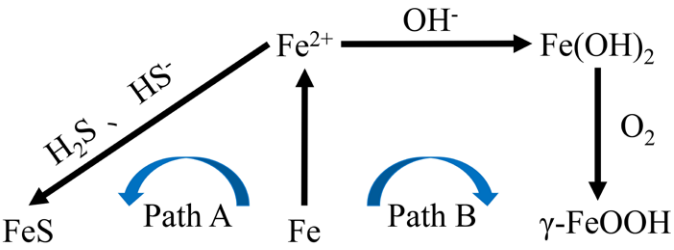

Fig. 8. The reaction network of carbon steel dissolution in a NaCl solution containing sulfide

It is well known that γ-FeOOH is a thermodynamically unstable corrosion product [6,39]. The instability of the corrosion products facilitates the ingress of oxygen into the coating/metal interface, promoting reduction reactions that generate OH^-, which, in turn, enhances the cathodic area.

As the concentration of sodium sulfide diminishes, XPS analyses were conducted on the corrosion products at the artificial defects during the later stages of immersion. In Fig. 9(e), the Fe $2p_{3/2}$ peak at 712.5 eV is assigned to Fe_2O_3 [41]. The above XPS results indicate that the corrosion products at the artificial defects are predominantly FeS. Potential reactions that may occur when the terminal electrode surface is immersed are outlined below [42, 43]:

$$FeS + 2H_2O \rightarrow \gamma\text{-FeOOH} + S^{2-} + 3H^+ + e^- \quad (15)$$

$$2FeS + 3H_2O \rightarrow Fe_2O_3 + 2S^{2-} + 6H^+ + 2e^- \quad (16)$$

The reversible reaction between FeS and H_2O not only facilitates the ingress of oxygen, leading to the formation of γ-FeOOH and the generation of cathodic current beneath the epoxy coating, but also contributes to the formation of a protective FeS layer on the bare steel surface, thereby further mitigating the corrosion of the exposed steel.

3.4. Corrosion characteristics of single electrode under organic coating

The current density changes of No. 59 and 87 single electrodes in WBE are shown in Fig. 10. The cathodic current density of the No. 59 and 87 electrodes is higher during the initial immersion phase. Following approximately 24 h of immersion, the cathodic current density diminishes. This phenomenon can be attributed to the limitation of the oxygen reduction reaction, induced by the presence of corrosion products in the bare steel region. However, the formation of loose corrosion products during the later stages of immersion accelerates the involvement of oxygen in the cathodic reduction reaction,

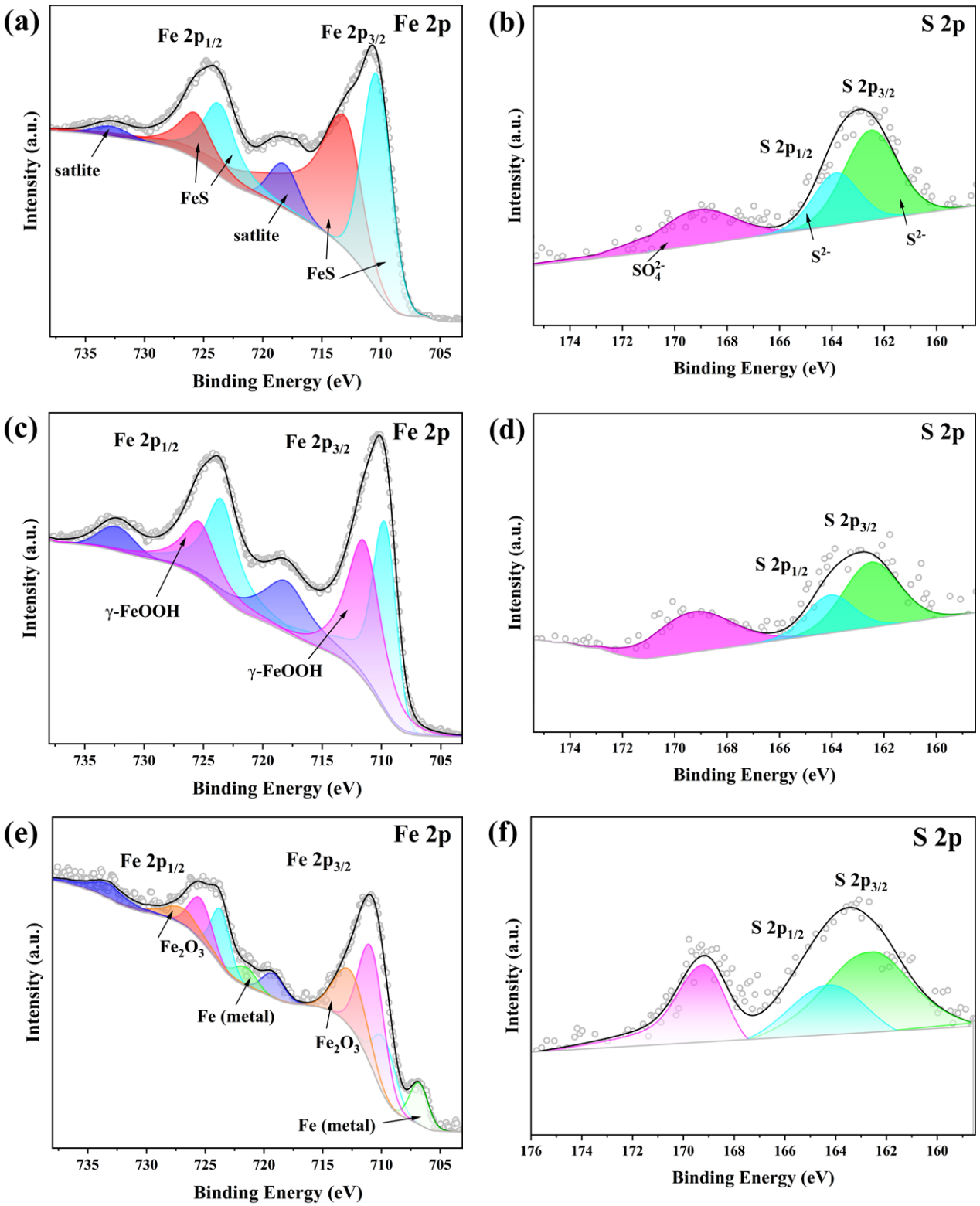

Fig. 9. High-resolution X-ray photoelectron spectroscopy plots of artificial defects in the wire beam electrode at different immersion stages: (a, b) early; (c, d) mid-stage; (e, f) late

ultimately resulting in a gradual increase in cathodic current. Notably, the absolute cathodic current density of the No. 59 electrode exceeded 1 μA/cm^2 after 108 h of immersion, and polarity reversal occurred after 324 h. The macroscopic surface morphology of the coating removed after immersion for 432 h is shown in Fig. 11(b). The surface of the No. 59 electrode is observed to be covered with yellow rust. The mechanism behind the layering of the epoxy coating on the WBE surface can be attributed to the prolonged influence of the cathodic current, which generates OH^- during the cathodic reaction. This leads to significant alkalization at the coating/metal interface, subsequently resulting in the delamination of the coated cathode

[18,22]. Electrolyte solutions can easily diffuse into the coating/metal interface area, causing active dissolution and destroying the protective effect of the coating. Yellow rust was also observed on other A36 electrodes. These findings provide robust support for the results obtained from the EIS characterization of the carbon steel and copper-nickel alloy deposits. The surface morphology of WBE without removing the coating is shown in Fig. 11(a). Correspondingly, bubbling can be seen on the surface of No. 59 electrode. It should be noted that blistering phenomenon also exists on the surface of the No. 60 electrode. For illustration, we focus on the No. 59 electrode. Upon removal of the coating, the surface of the No. 87 electrode exhibited black corrosion products. When the coating remains intact, mass transfer can only occur through the openings of the artificial defects. This process hinders the outward diffusion of Fe^{2+} from the coating. Consequently, the accumulation of surface corrosion products at the artificial defects ultimately results in the reduction of the corrosion product γ-FeOOH, driven by anodic erosion. The presence of black corrosion products confirms that γ-FeOOH participates in the reduction reaction to form Fe_3O_4. The possible reaction is shown below [22,44]. It should be noted that the absence of polarity reversal at the electrode with the artificial defect, despite the participation of the rust layer, may be due to the dominant active dissolution at the anode over the cathodic reduction reaction.

$$8\gamma\text{-FeOOH} + Fe^{2+} + 2e^- \rightarrow 3Fe_3O_4 + 4H_2O \qquad (17)$$

The change of current density with immersing time of No. 46 and 90 single electrodes in WBE is shown in Fig. 12. The No. 90 electrode exhibits a cathodic current during the intermediate immersion phase, with the absolute current density exceeding 1 μA/cm^2. With increasing immersion time, the cathodic current transitions into an anodic current. This phenomenon is attributed to cathodic delamination, induced by localized alkalinization. As shown in Fig. 11(a), bubbling is observed on the surface of the No. 90 electrode. The No. 46 electrode exhibited anodic current from 24 to 144 h, with current values ranging around 1 μA/cm^2. After removal of the coating, the surface remains bright, as depicted in Fig. 11(b). This observation aligns with the general phenomenon that, when A36 is coupled with B18 and immersed, the A36 surface undergoes preferential corrosion. Additionally, the surfaces of other B18 electrodes, such as No. 23 and 29, exhibit a light green color. XPS analysis was conducted on the surface composition of the B18 electrode, as illustrated in Fig. 13. After immersion in a sulfide-containing NaCl solution for 432 h, the surface is predominantly composed of Cu/Cu_2O

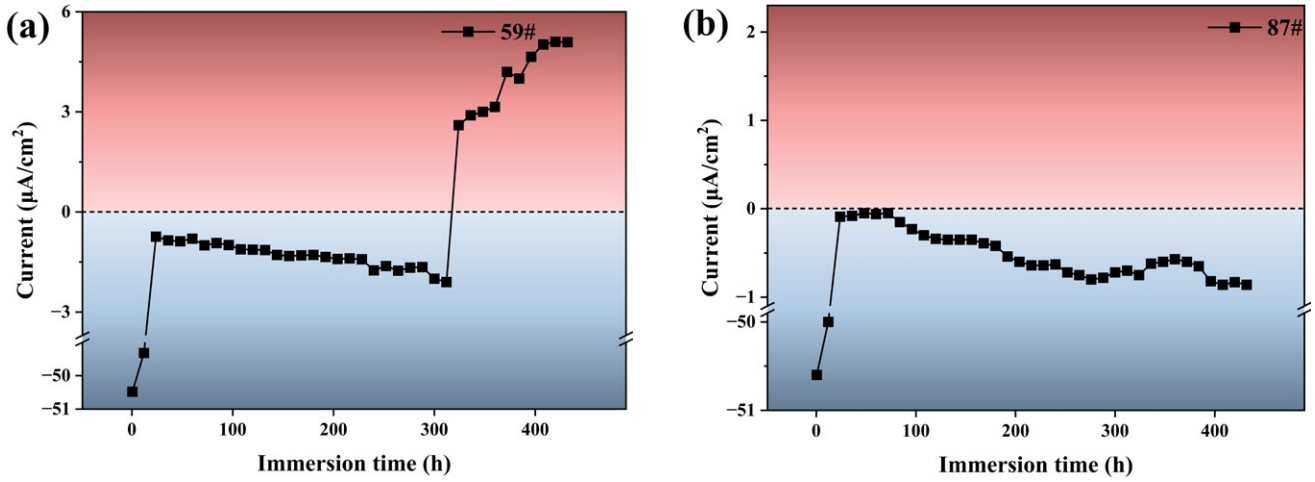

Fig. 10. Changes in current density of No. 59 and 87 single electrodes in wire beam electrode with immersion time

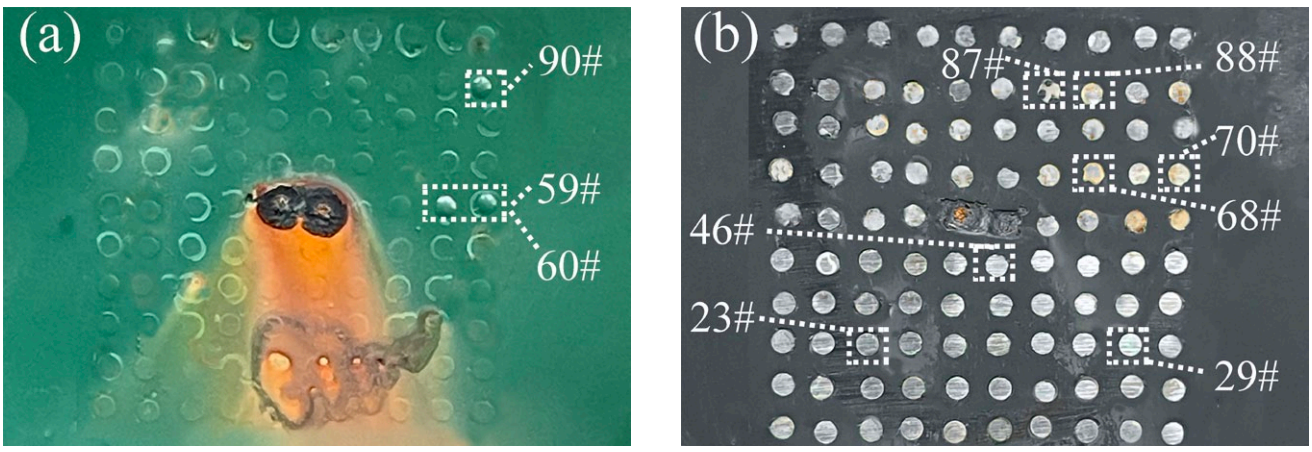

Fig. 11. Surface macroscopic morphology after wire beam electrode immersion for 432 h: (a) without coating removal, (b) after coating removal

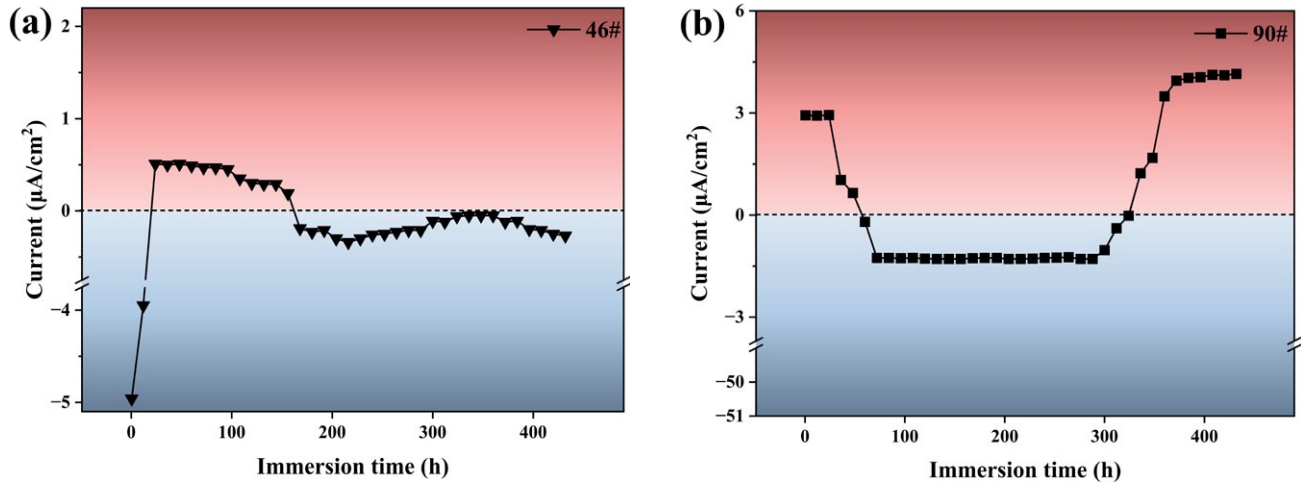

Fig. 12. Changes in current density of No. 46 and 90 single electrodes in wire beam electrode with immersion time

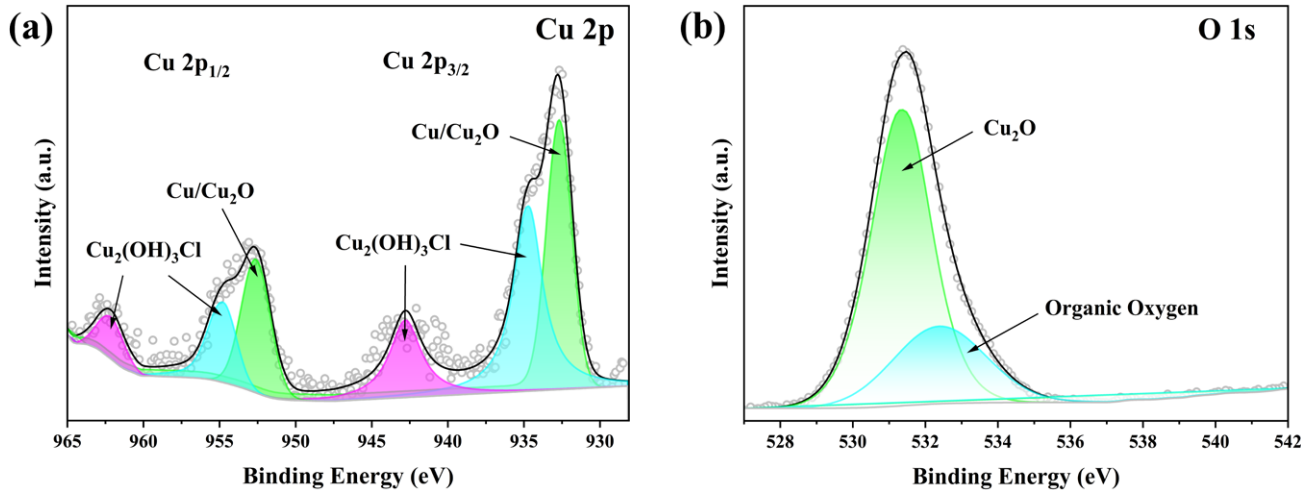

Fig. 13. High-resolution X-ray photoelectron spectroscopy plots on copper-nickel alloys at the final stage of immersion: (a) Cu 2p; (b) O 1s

(binding energy = 932.7 eV) and $Cu_2(OH)_3Cl$ (binding energy = 934.7 eV, 942.8 eV) [1]. In the corresponding O1s spectrum, the binding energy of Cu_2O is observed at 531.3 eV, while the peak at 532.4 eV corresponds to organic oxygen [1]. Given that the typical XPS analysis depth is 3-10 nm, and Ni is concentrated in the inner layers of the corrosion product film, no Ni 2p signal is detected. Both the outer copper species, $Cu_2(OH)_3Cl$, and the inner-layer Cu_2O maintain the chemical equilibrium of the corrosion product film, thereby verifying its protective effect on the substrate. The potential chemical reactions involved in the formation of corrosion product films are outlined below [9,31,45]. Among them, $CuCl_2^-$ acts as an intermediate substance and is adsorbed on the electrode surface through the reaction:

$$Cu + 2Cl^- \rightarrow CuCl_2^- + e^- \quad (18)$$

$$2CuCl_2^- + H_2O \rightarrow Cu_2O + 2H^+ + 4Cl^- \quad (19)$$

$$Cu_2O + Cl^- + 2H_2O + (1/2)O_2 \rightarrow Cu_2(OH)_3Cl + OH^- \quad (20)$$

The schematic diagram of the WBE corrosion process induced by artificial defects under epoxy coating is shown in Fig. 14.

4. Conclusions

(1) Throughout the entire immersion period, the carbon steel electrode at the artificial defect predominantly functions as the anode. In the early stages of immersion, active dissolution occurs rapidly on the electrode surface. With increasing immersion time, corrosion in the artificial defect area becomes influenced by the corrosion product film, which subsequently suppresses further corrosion.

(2) The carbon steel and copper-nickel alloys under the coating exhibit electrochemical inhomogeneity during galvanic corrosion in a NaCl solution containing sulfide.

(3) During galvanic corrosion in a sulfide-containing NaCl solution involving carbon steel and copper-nickel alloy, the extent of cathodic delamination in the carbon steel region is greater than in the copper-nickel alloy region. This phenomenon is primarily influenced by the electrochemical activity of the metals and the location of coating defects.

(4) During the later stages of immersion, polarity reversal from cathode to anode is observed on multiple electrodes within the carbon steel region. This phenomenon is primarily

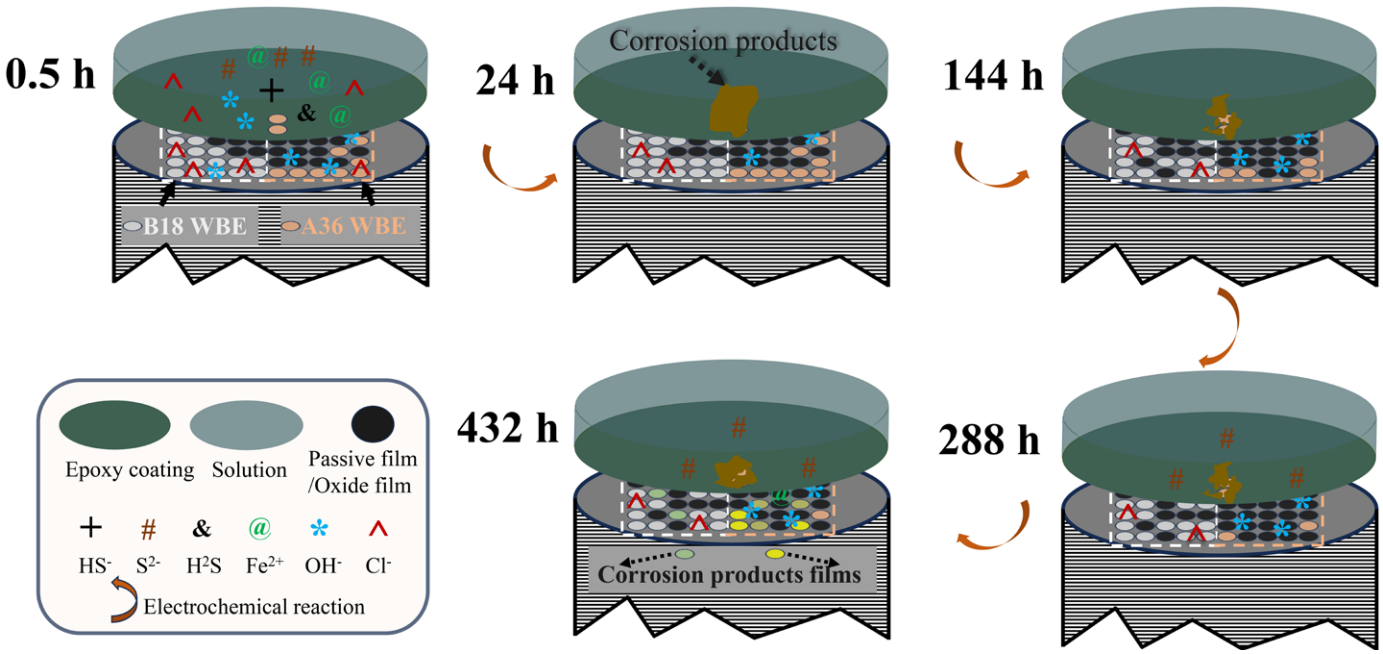

Fig. 14. Corrosion mechanism schematic diagram of galvanic couple in a NaCl solution containing sulfides

attributed to cathodic stratification on the electrode surface, which facilitates the erosion of corrosive ions. Another possible explanation lies in the microgalvanic effect between the two metals, which exacerbates the anodic active dissolution of carbon steel beneath the epoxy coating. Certain electrodes undergo polarity reversal from anode to cathode. This behavior can be attributed to the involvement of the corrosion product γ-FeOOH in the cathodic reduction reaction.

(5) The copper-nickel alloy remains consistently protected throughout the immersion period. This can be ascribed to the protective role of the surface corrosion product film (Cu_2O $Cu_2(OH)_3Cl$) and the microgalvanic effect.

Acknowledgements

This work was supported by the Special Funds for the Construction of an Innovative Province of Hunan (2019GK2231).

REFERENCE

[1] L. Wu, Y.T. Xu, A.L. Ma, L.M. Zhang, Y.G. Zheng, Influence of pre-immersion aeration conditions on corrosion product films and erosion-corrosion resistance of 90/10 and 70/30 copper-nickel tubes in 1 wt% NaCl solution. Corros. Sci. **228**, 111817 (2024). DOI: https://doi.org/10.1016/j.corsci.2024.111817

[2] J. Wang, H. Li, M. Du, M.X. Sun, L. Ma, Study on mechanism underlying the acceleration of pitting corrosion of B30 copper-nickel alloy by sulfate-reducing bacteria in seawater. Sci. Total Environ. **928**, 172645 (2024). DOI: https://doi.org/10.1016/j.scitotenv.2024.172645

[3] G.X. Li, H.Y. Xing, M. Du, M.X. Sun, L. Ma, Accelerated corrosion of 70/30 copper-nickel alloys in sulfide-polluted seawater environment by sulfide. J. Mater. Res. Technol. **30**, 8620 (2024). DOI: https://doi.org/10.1016/j.jmrt.2024.05.212

[4] T.Z. Jin, W.F. Zhang, N. Li, X.R. Liu, L. Han, W. Dai, Surface characterization and corrosion behavior of 90/10 copper-nickel alloy in marine environment. Materials **12**, 1869 (2019). DOI: https://doi.org/10.3390/ma12111869

[5] A.L. Ma, S.L. Jiang, Y.G. Zheng, W. Ke, Corrosion product film formed on the 90/10 copper-nickel tube in natural seawater: Composition/structure and formation mechanism. Corros. Sci. **91**, 245 (2015). DOI: https://doi.org/10.1016/j.corsci.2014.11.028

[6] Y.C. Liu, Z.B. Zheng, L. Xu, Z.B. Xu, F.X. Yin, K.H. Zheng, Unraveling the interfacial structure of TA2 titanium-A36 steel composite plate and its corrosion behavior in marine environment. Corros. Sci. **230**, 111923 (2024). DOI: https://doi.org/10.1016/j.corsci.2024.111923

[7] Z.X. Ye, L. Guan, Y. Li, J.X. Zhong, L.C. Liao, D.W. Xia, J.Y. Huang, Understanding the galvanic corrosion of Cu-Ni alloy/2205 DSS couple using electrochemical noise and microelectrochemical studies. Corros. Sci. **224**, 111512 (2023). DOI: https://doi.org/10.1016/j.corsci.2023.111512

[8] Y.A. Pu, Y.F. Cheng, W.W. Dou, Z.X. Xu, S. Hou, Y. Hou, S.G. Chen, Microbiologically influenced corrosion behavior of 70/30 Cu-Ni alloy exposed to carbon starvation environments with different aggressiveness: Pitting mechanism induced by Desulfovibrio vulgaris. Corros. Sci. **222**, 111427 (2023). DOI: https://doi.org/10.1016/j.corsci.2023.111427

[9] S.B. Hu, R. Liu, L. Liu, Y. Cui, F.H. Wang, Influence of temperature and hydrostatic pressure on the galvanic corrosion between 90/10 Cu-Ni and AISI 316L stainless steel. J. Mater. Res. Technol. **13**, 1402 (2021). DOI: https://doi.org/10.1016/j.jmrt.2021.05.067

[10] Q.N. Song, Y. Tong, N. Xu, S.Y. Sun, H.L. Li, Y.F. Bao, Y.F. Jiang, Z.B. Wang, Y.X. Qiao, Synergistic effect between cavitation erosion and corrosion for various copper alloys in sulphide-containing 3.5% NaCl solutions. Wear **450-451**, 203258 (2020).
DOI: https://doi.org/10.1016/j.wear.2020.203258

[11] Z.Y. Wei, D.D. Cui, Z. Wei, S. Hong, Effect of sulphide concentration on corrosion behaviors of HVOF-sprayed WC-Cr_3C_2-Ni and WC-Ni coatings. International Journal of Refractory Metals and Hard Materials **111**, 106104 (2023).
DOI: https://doi.org/10.1016/j.ijrmhm.2023.106104

[12] G. Šekularac, I. Milošev, Corrosion of aluminium alloy AlSi7Mg0.3 in artificial sea water with added sodium sulphide. Corros. Sci. **144**, 54 (2018).
DOI: https://doi.org/10.1016/j.corsci.2018.08.038

[13] K. Habib, A. Husain, Stress corrosion cracking of copper-nickel alloys in sulplxide polluted natural seawater at moderate temperatures. Desalination **97**, 29 (1994).

[14] M. Goldman, C. Tully, J.J. Noël, D.W. Shoesmith, The influence of sulphide, bicarbonate and carbonate on the electrochemistry of carbon steel in slightly alkaline solutions. Corros. Sci. **169**, 108607 (2020).
DOI: https://doi.org/10.1016/j.corsci.2020.108607

[15] H. Ju, Y.F. Yang, Y.F. Liu, S.F. Liu, J.Z. Duan, Y. Li, Mapping the galvanic corrosion of three metals coupled with a Wire Beam Electrode: The influence of temperature and relative geometrical position. Materials **11**, 357 (2018).
DOI: https://doi.org/10.3390/ma11030357

[16] J. Kou, D.X. Ma, Galvanic corrosion based on wire beam electrode technique: progress and prospects. Corros. Rev. **40**, 205 (2022).
DOI: https://doi.org/10.1515/corrrev-2021-0100

[17] G.A. Zhang, N. Yu, L.Y. Yang, X.P. Guo, Galvanic corrosion behavior of deposit-covered and uncovered carbon steel. Corros. Sci. **86**, 202 (2014).
DOI: https://doi.org/10.1016/j.corsci.2014.05.011

[18] J. Xie, Z.H. Lu, K. Zhou, C.P. Li, J.Y. Ma, B. Wang, K.S. Xu, H.T. Cui, J. Liu, Researches on corrosion behaviors of carbon steel/copper alloy couple under organic coating in static and flowing seawater. Prog. Org. Coat. **166**, 106793 (2022).
DOI: https://doi.org/10.1016/j.porgcoat.2022.106793

[19] C.R. Gu, J.Y. Hu, X.K. Zhong, Evidence of hydrogen gas evolution accelerating the cathodic coating delamination. Corros. Commun. **7**, 63 (2022).
DOI: https://doi.org/10.1016/j.corcom.2022.04.001

[20] J. Liu, Z.H. Lu, L.W. Zhang, C.P. Li, R. Ding, X.D. Zhao, P.Q. Zhang, B. Wang, H.T. Cui, Studies of corrosion behaviors of a carbon steel/copper-nickel alloy couple under epoxy coating with artificial defect in 3.5 wt.% NaCl solution using the WBE and EIS techniques. Prog. Org. Coat. **148**, 105909 (2020).
DOI: https://doi.org/10.1016/j.porgcoat.2020.105909

[21] C.C. Zhang, S.M. Li, J. Xiao, R. Wang, X.Y. Xu, J.H. Liu, M. Yu, Enhanced heat and corrosion resistance of organic silicone coatings by dual shielding effects of Zn powder. Electrochim. Acta **509**, 145329 (2025).
DOI: https://doi.org/10.1016/j.electacta.2024.145329

[22] Y. Li, Z.L. Feng, H. Guo, X.Y. Zhang, B. Fang, K. Zhou, B. Wang, J. Liu, Waterline corrosion behaviors of carbon steel covered by organic coating with artificial defects in seawater. Colloids Surf. A **681**, 132840 (2024).
DOI: https://doi.org/10.1016/j.colsurfa.2023.132840

[23] J.M. Sykes, Y. Xu, Electrochemical studies of galvanic action beneath organic coatings. Prog. Org. Coat. **74**, 320 (2012).
DOI: https://doi.org/10.1016/j.porgcoat.2012.01.009

[24] J.M. Sykes, Y. Xu. Investigation of electrochemical reactions beneath paint using a combination of methods. In: The Electrochemical Society, organizer. Fifth International Symposium on Advances in Corrosion Protection by Organic Coatings; 2010; New Jersey, United States. (vol. 24, 1). p. 137-146.
DOI: https://doi.org/10.1149/1.3453613

[25] https://www.doc88.com/p-57039437498107.html

[26] https://max.book118.com/html/2024/0103/5043140002011034.shtm

[27] S. Gudić, L. Vrsalović, A. Matošin, J. Krolo, E.E. Oguzie, A. Nagode, Corrosion behavior of stainless steel in seawater in the presence of sulfide. Applied Sciences **13**, 4366 (2023).
DOI: https://doi.org/10.3390/app13074366

[28] R. Abdel-Karim, M.A. Farag, H.a.-A. Ahmed, S. El-Raghy, Corrosion resistance of API5L X52 carbon steel in sulfide polluted environments. Mater. Sci. Appl. **07**, 39 (2016).
DOI: https://doi.org/10.4236/msa.2016.71005

[29] N.S. Al-Mamun, W. Haider, I. Shabib, Corrosion resistance of additively manufactured 316L stainless steel in chloride-thiosulfate environment. Electrochim. Acta **362**, 137039 (2020).
DOI: https://doi.org/10.1016/j.electacta.2020.137039

[30] X. Gai, Y. Bai, S.J. Li, W.T. Hou, Y.L. Hao, X. Zhang, Y. Han, R. Yang, R.D.K. Misra, In-situ monitoring of the electrochemical corrosion behavior in fluoride environment of cellular structured Ti6Al4V alloy fabricated by electron beam melting. Corros. Sci. **181**, 109258 (2021).
DOI: https://doi.org/10.1016/j.corsci.2021.109258

[31] Y. Hou, Y.N. Pu, S.G. Chen, Z.H. Guo, S. Hou, W. Wang, Insight into the corrosion susceptibility and failure mechanism of Cu-Ni alloy pipeline welded joints in simulated marine environment. Engineering Failure Analysis **160**, 108184 (2024).
DOI: https://doi.org/10.1016/j.engfailanal.2024.108184

[32] X. Yu, J.G. Liu, H.L. Jiang, G. Cui, X.M. Luo, The formation of pitting under dynamic DC interference: Corrosion product film defects or passive film induction. Corros. Sci. **231**, 111961 (2024).
DOI: https://doi.org/10.1016/j.corsci.2024.111961

[33] T. Tichter, J. Schneider, C. Roth, Convolutive modeling of cyclic voltammetry, AC-voltammetry, sine wave voltammetry and impedance spectroscopy with interfacial CPE behaviour and uncompensated ohmic resistances: A Unified Theory. Electrochim. Acta **393**, 139006 (2021).
DOI: https://doi.org/10.1016/j.electacta.2021.139006

[34] B.Y. Chang, Conversion of a constant phase element to an equivalent capacitor. Journal of Electrochemical Science and Technology **11**, 318 (2020).
DOI: https://doi.org/10.33961/jecst.2020.00815

[35] D. Kong, Y. Wang, W. Zhang, W. Wang, X. Liu, J. Wang, Correlation between electrochemical impedance and current distribution of carbon steel under organic coating. Mater. Corros. **63**, 475 (2011). DOI: https://doi.org/10.1002/maco.201006035

[36] L. Yang, Z.Y. Liu, X.J. Yang, X.X. Xu, X.Q. Cheng, X.G. Li, Behavior and evaluation of stress corrosion cracking of typical anchor bolt steel in simulated crevice environment. J. Mater. Res. Technol. **25**, 7430 (2023).
DOI: https://doi.org/10.1016/j.jmrt.2023.07.149

[37] L.Y. Yang, D.L. Zhang, H.M. Fan, X.K. Fu, R.Z. Yan, Z.Y. Wei, H.L. Wu, In-situ electrochemical testing and fluid dynamics simulation of pipeline defects under flow accelerated corrosion. Experimental Thermal and Fluid Science **150**, 111048 (2024). DOI: https://doi.org/10.1016/j.expthermflusci.2023.111048

[38] F.X. Shi, L. Zhang, J.W. Yang, M.X. Lu, J.H. Ding, H. Li, Polymorphous FeS corrosion products of pipeline steel under highly sour conditions. Corros. Sci. **102**, 103 (2016).
DOI: https://doi.org/10.1016/j.corsci.2015.09.024

[39] Y. Zhang, Y.Z. Yang, K. Yang, L.S. Yu, The effect of acetic acid on the crevice corrosion of P110 steel in simulated oilfield produced water. Int. J. Electrochem. Sci. **19**, 100433 (2024).
DOI: https://doi.org/10.1016/j.ijoes.2023.100433

[40] T.S. Zhang, Z.Y. Wang, Y.B. Qiu, T. Iftikhar, H.F. Liu, "Electrons-siphoning" of sulfate reducing bacteria biofilm induced sharp depletion of Al--Zn--In--Mg--Si sacrificial anode in the galvanic corrosion coupled with carbon steel. Corros. Sci. **216**, 111103 (2023). DOI: https://doi.org/10.1016/j.corsci.2023.111103

[41] H. Liu, J. Chen, X. Tian, Z. Wang, Y. Zhang, Y. Yan, Effect of fretting regimes on the fretting corrosion behavior of stainless steel in artificial crevices. Corros. Sci. **231**, 111984 (2024).
DOI: https://doi.org/10.1016/j.corsci.2024.111984

[42] R.J. Biernat, R.G. Robins, High-temperature potential/pH diagrams for the iron-water and iron-water-sulphur systems. Electrochim. Acta **17**, 1261 (1972).

[43] P.K. Baranwal, P.V. Rajaraman, Electrochemical investigation on effect of sodium thiosulfate ($Na_2S_2O_3$) and ammonium chloride (NH_4Cl) on carbon steel corrosion. J. Mater. Res. Technol. **8**, (2019). DOI: https://doi.org/10.1016/j.jmrt.2018.05.029

[44] J. Liu, L.W. Zhang, X.L. Mu, P.Q. Zhang, Studies of electrochemical corrosion of low alloy steel under epoxy coating exposed to natural seawater using the WBE and EIS techniques. Prog. Org. Coat. **111**, 315 (2017).
DOI: https://doi.org/10.1016/j.porgcoat.2017.06.012

[45] T.T. Xia, L.F. Zeng, X.H. Zhang, J. Liu, W.L. Zhang, T.X. Liang, B. Yang, Enhanced corrosion resistance of a Cu-10Ni alloy in a 3.5 wt.% NaCl solution by means of ultrasonic surface rolling treatment. Surf. Coat. Technol. **363**, 390 (2019).
DOI: https://doi.org/10.1016/j.surfcoat.2019.02.039